Lappeenranta
University of Technology

Saku Levikari

DETECTION OF CRACKS - ACOUSTIC EXPERIMENTS ON MULTILAYER CERAMIC CAPACITORS

Abstract

In this thesis, it is shown that damaged Multilayer Ceramic Capacitors (MLCCs) can be acoustically identified in a non-destructive manner. This is done by utilizing the piezoelectric behavior of the ceramic dielectric, which causes the capacitor to physically deform when voltage is applied. An acoustic response is obtained by driving an MLCC with pulse wave sweep over a wide frequency range, and measuring mechanical vibrations directly from the capacitor using a piezoelectric point contact sensor. Structural damage in the MLCC causes characteristic changes in the acoustic response, which can be algorithmically detected. An algorithm is introduced, in which an acoustic envelope is obtained from an MLCC and compared with a statistical reference envelope obtained from a sample of intact MLCCs. The results show that a damaged MLCC can be identified based on its acoustic emission.

Tiivistelmä

Tässä työssä osoitetaan, että vialliset monikerroksiset keraamiset kondensaattorit
(Multilayer Ceramic Capacitor, MLCC) voidaan tunnistaa akustisesti kondensaattoria vahingoittamatta. Tämä tapahtuu hyödyntämällä kondensaattorin keraamisen väliaineen pietsosähköisyyttä, joka aiheuttaa kondensaattorin rungon deformoitumisen kun jännite kytketään komponentin yli. Kondensaattorista mitataan akustinen vaste syöttämällä komponenttiin pulssimuotoista jännitettä. Jännitteen taajuutta nostetaan lineaarisesti laajan taajuusalueen yli, mitaten samalla kondensaattorin rungon mekaanisia värähtelyjä pietsosähköisellä pintakontaktianturilla. Kondensaattorissa olevat mekaaniset vauriot aiheuttavat komponentin akustiseen vasteeseen muutoksia, jotka voidaan havaita tarkoitukseen kehitetyllä algortmilla. Työssä esitellään algoritmi, joka laskee kondensaattorin akustisesta vasteesta verhokäytän, ja vertaa sitä ehjien kondensaattorien vasteista muodostettuun referenssiverhokäyrään. Tulokset osoittavat, että vikaantunut kondensaattori voidaan tunnistaa akustisien emissioiden perusteella.

Acknowledgements

Contents

Nomenclature

Latin alphabet

A	Area
a	Length of a plate
b	Width of a plate
C	Capacitance
D	Duty cycle
D	Flexural rigidity
d_{pk}	Piezoelectric constant tensor
$\vec{\mathbf{E}}$	Electric field
E	Electric field strength
F	Force, temporal component of deflection field of a plate
f	Frequency
$\mathcal{H}(\cdot)$	Hilbert transform
H	Observation matrix
h	Half-thickness of a plate
L_{GLS}	Difference value of two curves, one GLS-fitted into another
N	Number of observations
N_{DS}	Downsampling factor
$\vec{\mathbf{P}}$	Polarization field
P	polarization
Q	Total electric charge
q	Electric charge
$\mathbf{S}$, S_{ij}	Strain
S	Surface
s^E_{pq}	Electric compliance tensor
T_q	Stress
U	Voltage
v	Error vector
W	Weighting matrix
w	Deflection field of a plate
W_{x_1,x_2}	Spatial component of deflection field of a plate

Greek alphabet

ϵ	dielectric constant
γ_E	Young's modulus
ν	Poisson's ratio
ω	Angular frequency
ω_{mn}	Resonance frequencies of a plate
σ	Surface charge density

θ Observation model parameter for LS-fitting

Subscripts

DS	Downsampling
GLS	Generalized Least Squares
i, j, p, q	Tensor components
x_1, x_2	Location on a plate surface

Abbreviations

AC	Alternating Current
$BaTiO_3$	Barium Titanate
DC	Direct Current
FFT	Fast Fourier Transform
lpf	Low-pass filter
MLCC	Multilayer Ceramic Capacitor
Std	Standard deviation
TiO_3	Titanium Oxide

1   Introduction

Multilayer Ceramic Capacitors (MLCCs) are widely used in industry because of their high capacitance per volume and favorable electrical characteristics (Ko et al., 2014). Approximately 80% of all currently manufactured capacitors are chip-type MLCCs (TDK Corporation, 2016). MLCCs are, however, prone to mechanical damage and subsequent failure because of fragility of the ceramic dielectric. Typical mechanical defects in MLCCs include cracks, voids and delaminations. Voids typically do not expand over time, but they may cause cracks and delaminations to expand (Adams, 2014).

Figure 1.1 shows a cross-section of an MLCC with a typical crack within the dielectric near the end termination, cutting a portion of the inner electrodes. Such a defect is often caused in the production, or as a result of mishandling or bending of the Printed Circuit Board (PCB) the MLCC is attached to (Krieger et al., 2006). Thermal stresses during manufacturing or soldering process are also associated with the emergence of these defects (Huang et al., 2015). If a defect is sufficiently large, it may shorten the operational life of the capacitor, lower the capacitance value or cause the capacitor to short circuit. (Kahn and Checkaneck, 1983). Water getting inside the MLCC trough a crack may also cause degradation of the ceramic dielectric. The degradation results from electrolysis within the dielectric material when voltage is applied to the capacitor (Wang et al., 2003).

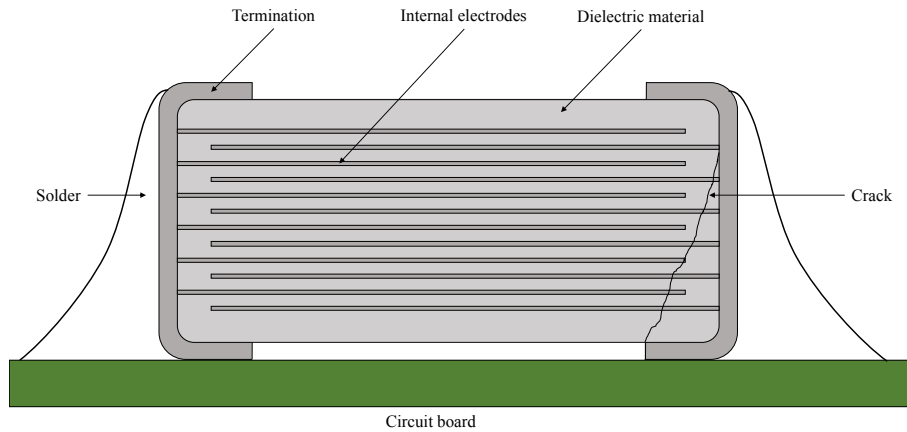

Figure 1.1: Structure of a typical Multilayer Ceramic Capacitor with a crack in the dielectric material cutting a part of the inner electrodes

The aforementioned defects are often not recognized in production, but start affecting the performance of the capacitor in operational use (Kahn and Checkaneck, 1983). Hence, there is a need for detecting such defects before the final product is sold.

Microsectioning is a commonly used destructive method for detecting and localizing mechanical defects in MLCCs. Multiple non-destructive methods have also been developed:

Kahn and Checkaneck (1983) introduced a method in which an MLCC is placed under a mechanical ram with increasing downward force on the MLCC. Acoustic signals emitted by the cracks in the dielectric are counted using a transducer mounted on the ram. The authors suggested that the method could be used for statistical screening of a sample of MLCCs taken from a production line.

Acoustic microscopy and opto-acoustic microscopy, i.e. measurement of laser-induced acoustic emissions, have been studied for defect detection purposes in the form of scanning laser acoustic microscopy and C-mode scanning acoustic microscopy. (Commare, 1993)

Bechou et al. (1996) introduced a method for defect detection and localization based on electromechanical resonances of an MLCC. The method consisted of impedance analysis of the MLCC under DC bias voltage. The same method was used by Krieger et al. (2006). This method relies on the piezoelectric deformation of the MLCC under DC bias voltage. The impedance of the MLCC is analyzed over a wide frequency range, covering the mechanical resonance frequencies of the MLCC. Mechanical resonances and possible defects cause peaks in the impedance curve, from which they can be detected.

Chan et al. (1995) presented a method of defect detection, which is based on laser speckle pattern analysis. A local short circuit between electrodes in an MLCC causes the temperature to rise at the location of the defect, leading to thermal deformation. This deformation can be detected by comparing laser speckle images of the MLCC under voltage and under no voltage. This method requires a more complicated test setup than the one presented in this thesis, but according to authors, is suitable for *in situ* measurements. This method requires voltage applied to the capacitor. Erdahl and Ume (2004) demonstrated a method for MLCC quality inspection, in which the MLCC was excited into vibration using a pulsed laser, and the vibration was measured using laser interferometry. This method is very similar to the method presented in this thesis in such way that the physical vibration of the top side of the MLCC is measured. The laser interferometry is capable of measuring higher frequencies than other methods, including the one presented in this thesis, but requires more complicated measurement setup. This method requires no voltage application to the MLCC.

Krieger et al. (2006) used audio range microphone to obtain acoustic emissions from an MLCC attached to a PCB. Similar method was tested out in this thesis. According to study by Ko et al. (2014), the audio range frequencies are, however, mainly result of the vibration of the circuit board. Thus, the audio-range acoustic emissions are mainly dictated by the properties of the PCB, although the the structural condition of the capacitor probably also has some contribution to the acoustic emissions

obtained.

Other non-destructive methods for measuring vibrations and structural condition of an MLCC are scanning laser Doppler vibrometer (Ko et al., 2014), computer tomography using ultrasound, and X-ray imaging. The usability of neutron radiography has also been studied (Kieran, 1981).

This thesis presents a nondestructive method of characterizing soldered multilayer ceramic capacitors acoustically. First, an MLCC is subjected to frequency-swept pulse wave. During the frequency sweep, MLCC generates acoustic emissions, which are observed using a piezoelectric point contact sensor placed on top of the capacitor. The acoustic response of the MLCC is then analyzed for anomalies which might indicate damage in the capacitor. The advantages of the method presented in this thesis are:

Simplicity
> The measurement equipment required for this method only requires a point contact sensor and an amplifier alongside a signal generator and an oscilloscope.

Speed
> Measuring one MLCC takes less than a minute. The measurement speed is limited mainly by manual placement of the point contact sensor and the oscilloscope's data transfer rate.

Ability to recognize different types of defects
> This method is capable of recognizing mechanical defects in both the dielectric medium and near the solder joints.

The disadvantages of this method are sensitivity to Electromagnetic Interference (EMI) and variations in the physical contact between the point contact sensor and the MLCC. Both of these cause bias when comparing the responses of MLCCs. Thus far this method is only suitable for offline measurements, because a measured capacitor has to be driven with sufficiently high voltage.

The acoustic approach presented in this thesis has been a subject for further study. It has been shown that damage in MLCCs indeed correlates with the acoustic emission metrics presented in this thesis (Levikari et al., 2018a). A Support Vector Machine classifier has been succcessfully demonstrated for classification of MLCC acoustic emissions (Levikari et al., 2017). The acoustic method presented in this thesis has also been used to construct an open MLCC acoustic data set (Levikari et al., 2018b).

1.1 Goal of this study

The aim of this study is to find a method for detecting defects in multilayer ceramic capacitors based on acoustic emissions. This study focuses on MLCCs of type II, i.e.

high-permittivity capacitors in which barium titanate ($BaTiO_3$) is typically used as the dielectric material. Different methods for obtaining acoustic data from MLCCs are compared, and analysis methods for acoustic data are developed and compared with each other.

An MLCC itself cannot generate significant acoustic response within audio frequency range; instead, the vibrating PCB is the main source of MLCC-related audible noise (Ko et al., 2014). Obtaining acoustic emissions using a microphone typically limits the frequency range to audible frequencies, and the properties of the PCB are likely to dominate the acoustic response. In order to bypass the contribution of the PCB, a method for obtaining acoustic emissions directly from the MLCC is presented.

1.2   Research questions and contributions

The contributions and associated research questions of this thesis are:

Verification of acoustic method
Is it possible to obtain information on the structural condition of an MLCC capacitor based on acoustic response?

Development of methods and instrumentation
What kind of methods and instrumentation are needed to yield measurements that are repeatable, reliable and sensitive enough for the acoustic monitoring of MLCCs?

Development of method of analysis
What kind of method of analysis is able to discriminate between valid and cracked MLCCs?

2 Physics of multilayer ceramic capacitors

Ceramic capacitors are classified under three types, shown in Table 2.1. The method presented in this thesis is based on measuring the mechanical motion of Type II Multilayer Ceramic Capacitors. This motion is caused by piezoelectric behavior of barium titanate ($BaTiO_3$) used as dielectric in Type II MLCCs. There are no notable piezoelectric effects in capacitors of Type I (Prymak, 2006). Because $SrTiO_3$ also exhibits piezoelectric behavior (Furuta and Miura, 2010), this method might also be applicable in some form to Type III capacitors.

2.1 Dynamics of MLCCs

Structure of a typical MLCC is presented in fig. 1.1 (see page 9). An MLCC can be expected to have multiple mechanical resonant frequencies, which depend on the structure, material properties and physical dimensions of the capacitor and its end terminations. Because of the relatively complex structure of an MLCC, obtaining closed-form solutions for the mechanical resonances is infeasible. The mechanical behavior and resonances of MLCCs have been studied previously by Ahmar and Wiese (2015) and Ko et al. (2014) using finite element method. The fundamental mechanical resonance frequencies of the MLCC in that particular study are in MHz-range. Previous studies suggest that the absence of audio-range mechanical resonances, in conjunction with the small physical size of MLCCs, means that the capacitor itself creates no significant audible noise. (Ko et al., 2014)

2.1.1 Piezoelectric behaviour of MLCCs

The mechanical deformation of an MLCC arises from the piezoelectric properties of barium titanate ($BaTiO_3$) used as dielectric in MLCCs. In room temperature, barium titanate has tetragonal crystalline structure which consists of grains less than a micrometer in size. The grains are divided into domains, in each of which the crystals share the same polarization, known as the spontaneous polarization. The dielectric constant ϵ relates to the polarization P of a medium as (Lee and

Table 2.1: Classification of ceramic capacitors by dielectric material. Based on TDK Corporation (2016)

Type	Dielectric material
I (Low permittivity)	TiO_2 etc.
II (High permittivity)	$BaTiO_3$ etc.
III (Semiconductor)	$BaTiO_3$, $SrTiO_3$ etc.

Aksay, 2001)

$$\epsilon \approx \frac{P}{\epsilon_0 + E}. \tag{2.1}$$

Below Curie-point and under no external electric field E, the grain domains of the BaTiO$_3$ are spontaneously polarized. Under weak electric field, the polarization of the domains is easily reversed. The polarization reversal by the electric field yields higher ϵ and thus, higher capacitance. (Skelly and Waugh, 2009).

Applying voltage bias over an MLCC causes net polarization over the domains of the dielectric, resulting in deformation of the dielectric (Yang, 2005). This phenomenon is called the inverse piezoelectric effect (Ousten et al., 1998). When high electric field is applied to the material, the reversal of the polarization in the grains becomes more difficult, and the net polarization essentially reaches its saturation. This causes decrease in capacitance in MLCCs under DC bias voltage. (Skelly and Waugh, 2009).

Figure 2.1 shows the directions of the electric fields and strains inside a capacitor. If a surface S that encloses one electrode with charge $q_{enclosed}$ is formed (Figure 2.1), then according to Gauss's law

$$\oiint_S \vec{\mathbf{E}} \cdot d\vec{\mathbf{S}} = \frac{q_{enclosed}}{\epsilon} \tag{2.2}$$

$$\Rightarrow E = \frac{q_{enclosed}}{\epsilon S} \tag{2.3}$$

on surfaces where $\vec{\mathbf{E}} \parallel d\vec{\mathbf{S}}$, and $E = 0$ elsewhere. In an MLCC with n layers of an area A, each electrode has an approximate charge of $q_{enclosed} = \frac{Q}{n/2}$, where Q is the total charge of a terminal. The electric field inside the dielectric is then

$$E = \frac{2Q}{n\epsilon A}. \tag{2.4}$$

The total capacitance of an MLCC is

$$C = \frac{Q}{U}. \tag{2.5}$$

From Equations (2.4) and (2.5) is found that

$$E = \frac{2CU}{n\epsilon A}. \tag{2.6}$$

When piezoelectric material is subjected to external electric field $\vec{\mathbf{E}} = (E_1, E_2, E_3)$, the material experiences deformation. The strain $\mathbf{S} = S_{ij}$ in the material is described in tensor notation as

$$S_p = s_{pq}^E T_q + d_{pk} E_k \tag{2.7}$$

(Dahiya, 2013), where s_{pq}^E is the electric compliance tensor at constant electric field, T_q is the stress the material is subjected to, and d_{pk} is the piezoelectric constant

tensor (IEE, 1987). The values of s_{pq}^E and d_{pk} for barium titanate are well known (Zgonik et al., 1994).

The electric field between the internal electrodes of a multilayer capacitor can be assumed to be homogeneous and perpendicular to the electrode plates. Assuming $\vec{\mathbf{E}} = (0, 0, E_3)$ and no external stress applied, the strain in the direction of the electric field becomes

$$S_3 = d_{333}E_3 \tag{2.8}$$

(IRE, 1949). According to (2.8), the strain and subsequent motion of the MLCC occurs mainly in the direction of the surface normal of the PCB, facilitating the measurement from the top cover of the capacitor.

From Eqs. (2.8) and (2.6) is obtained that the strain inside the dielectric material is

$$S_3 = d_{333}\frac{CU}{A\epsilon}. \tag{2.9}$$

Thus, the strain inside a ceramic capacitor is higher if the capacitance or voltage is increased, or if the electrode surface area is decreased. A more detailed study on the strains inside an MLCC with closed-form solutions has been made by Hsueh and Ferber (2002).
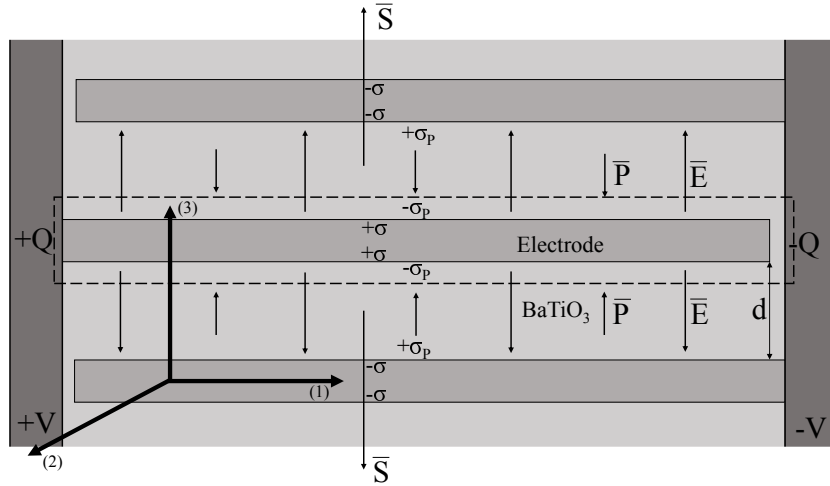
Figure 2.1: Electric fields inside an MLCC. When voltage is applied to end terminations, surface charge densities σ are formed on the electrode plates, creating electric field $\vec{\mathbf{E}}$ between the plates. The electric field causes $BaTiO_3$ to polarize, creating polarization field $\vec{\mathbf{P}}$ antiparallel to the field $\vec{\mathbf{E}}$. As $BaTiO_3$ polarizes, its crystalline structure is altered, creating strain $\vec{\mathbf{S}}$. The dashed line around the center electrode represents a Gauss surface, enclosing a total charge of $q_{enclosed}$.

2.2 Acoustic emissions from PCB

2.2.1 Mechanical force transfer

The kinetic energy of an MLCC is translated into the PCB via solder joints of the MLCC. The reverse piezoelectric effect creates strain and mechanical displacement along the poling axis. This movement is translated into transverse motion of the MLCC, which in turn creates torque on the PCB. (Ko et al., 2014)

2.2.2 Vibrational dynamics of Printed Circuit Boards

The vibrational motion of a plate can be described using Kirchoff-Love plate equations (Love, 1888), which are a commonly used model for small-amplitude vibrations of thin plates. Because the thickness of a PCB is typically very small compared to its other dimensions, the PCB is assumed to behave like a rectangular Kirchoff-Love plate with width $a = 39.0\,\mathrm{cm}$, length $b = 30.4\,\mathrm{cm}$ and thickness $2h = 1.55\,\mathrm{mm}$. The deflection field w of the plate, separated into spatial and temporal components W and F, is then

$$w(x_1, x_2, t) = W(x_1, x_2)F(t) \tag{2.10}$$

where the force acting on the plate is of the form

$$F(t) = Ae^{i\omega t} + Be^{-i\omega t}. \tag{2.11}$$

If a PCB is approximated with a Kirchoff-Love-plate with isotropic material properties and simply supported on all sides, the harmonic modes ω_{mn} are obtained by (Reddy, 2007)

$$\omega_{mn} = \frac{\pi^2}{b^2}\sqrt{\frac{D}{\rho h}}\left(m^2\frac{b^2}{a^2} + n^2\right). \tag{2.12}$$

Using Young's modulus γ_E as an average of the lengthwise value $24 \cdot 10^9$ Pa and cross-wise value $21 \cdot 10^9$ Pa, and Poisson's ratio ν as an average of lengthwise 0.136 and cross-wise 0.118, the flexural rigidity of FR-4 is approximately $D = \frac{\gamma_E h^3}{12(1-\nu^2)} \approx 7.8$. From eq. (2.12), it is obtained that the PCB has a fundamental mode ω_{11} at a frequency of 278.8 Hz. It is also seen that the PCB has its first 10 modes at frequencies below 2.5 kHz. These frequencies are well below of the resonance frequencies of the MLCCs, which are in the MHz-range.

3 Experiments

3.1 Measuring Acoustic Emissions from MLCCs

The main goal of the experiments was to obtain acoustic information from the MLCCs. Initially, two ways of measuring acoustic emissions were taken into consideration:

The indirect method
  In this method, acoustic emissions are measured from the PCB the MLCC is attached to. Driving the MLCC with AC voltage causes the MLCC to create mechanical vibrations. These vibrations are transmitted to the PCB, from which they can be measured, for example, with a microphone (Ko et al., 2014), or a point contact sensor.

The direct method
  In this method, the MLCC is driven with AC voltage, causing the MLCC to vibrate mechanically. These vibrations are measured directly from the capacitor using a point contact sensor.

The feasibility of obtaining acoustic information via the indirect method was studied at the beginning of this project. It was observed that with this method, the characteristics of the acoustic signal are heavily dependent on the location and distance of the sensor or microphone from the PCB. The mass, physical dimensions and material properties of the PCB determine the possible vibrational modes, as described in eq. (2.12).

To remove the effects of sensor placement and the vibration of the PCB, the direct method was selected for this thesis. Preliminary experiments show that the mechanical vibration amplitude of the PCB is very small on frequencies above 50 kHz (Fig. 4.12) and thus, the PCB has practically no contribution to the acoustic data obtained directly from the MLCC.

To minimize the effect of any external vibrations which could affect the measurements (such as background acoustic noise), the measurements were performed in an anechoic room. The main source of disturbances in the measurement data is EMI, for which the main cause is the measurement equipment.

3.2 Instrumentation and equipment

To generate acoustic response over a wide range of frequencies, the MLCCs were driven with pulse wave frequency sweeps, or chirps, using an Agilent 33250A signal generator. The chirps were 100 ms in duration, with frequency linearly increasing from 100 Hz to 2 MHz and with voltage of ± 10 V_{peak}. Duty cycle was set to signal

generator's maximum of D = 80%, as this was observed to maximize the ampli-
tude of the acoustic response. Figure 3.1 shows the frequency content of an ideal
pulse wave, which has power distributed over a wide range of harmonic frequencies.
Driving an MLCC with a pulse wave was observed to create significantly higher
acoustic response than a sine wave. Because a pulse wave consists of a high number
of harmonics, the obtained acoustic response also contains resonance peaks caused
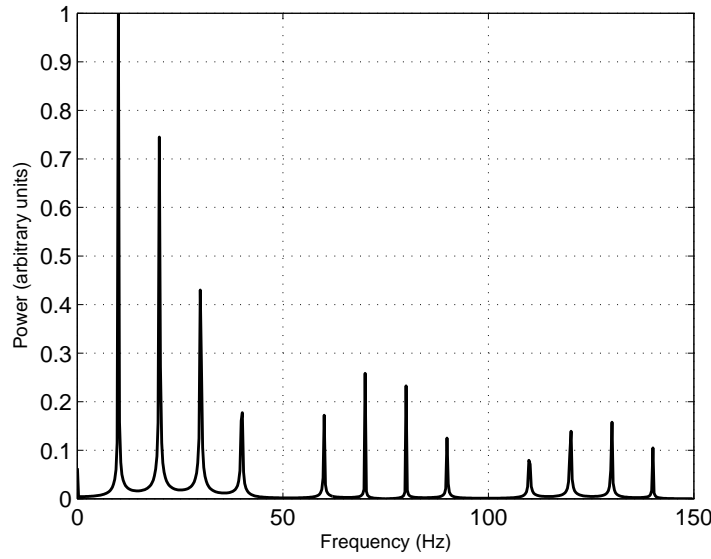by higher harmonics of the pulse wave signal.

Figure 3.1: A 1024-point FFT of a pulse wave with frequency of 10 Hz and duty cycle of
80 %

The acoustic response of the MLCC was picked up using a KRN point contact sensor
placed on top of the MLCC. The signal from the point contact sensor was amplified
using a KRN preamplifier. Specifications of the point contact sensor and preamplifier
are shown in Table 3.1. The output of the preamplifier was connected to a Keysight
InfiniiVision MSO-X 4104A Mixed Signal Oscilloscope. The measurement data was
the processed in Matlab.

The sensor was placed in a 3D-printed fixture (Fig. 3.2) to provide repeatable weight
and contact on MLCCs under examination. The tip of the sensor was covered with
Kapton-tape to prevent shorting the MLCC via its end terminations. The sensor
was used because it had the widest frequency range of the sensors readily available.
The measurement setup assembled in the anechoic room is shown in figures 3.3 and
3.4. An acoustic wall seen in figure 3.3 was assembled between the test board setup
and the rest of the measurement equipment to block the acoustic noise caused by
the oscilloscope and the signal generator.

Table 3.1: Specifications of the point contact sensor and preamplifier

---

Point contact sensor
> Model: KRNBB-PC Broadband point contact sensor
> Manufacturer: KRN Services
> Design: Conical piezoelectric crystal, built-in JFET (Mhamdi et al., 2015).
> Sensitivity: 15mV/nm $\pm$ 4dB over a frequency range 20 kHz – 1 MHz
> Maximum frequency: 2.5 MHz
> (KRN, 2015)

Preamplifier
> Model: AMP-1BB-J single channel broadband preamplifier
> Manufacturer: KRN Services
> Bandwidth: 3 dB over a frequency range 18.2 kHz – 2.0 MHz
> Gain: 28.1 dB at a frequency of 300 kHz
> (KRN, 2014)

3.3   MLCC measurement procedure

Acoustic measurements were performed on each MLCC individually. The test boards were characterized by measuring voltage chirp response of each MLCC on the board. Each board was characterized twice:

1. **Characterization of intact board**
   Each individual MLCC on the intact board was characterized to obtain reference data

2. **Bending of the board**
   The boards were bent using different strain levels. One pair of Boards 1 and 2 was subjected to strain of 6000 μstr, and another to strain of 4300μstr for Board 1 and 5800μstr for Board 2.

3. **Characterization of the bent board**
   Each MLCC on the board was characterized after the bending in order to find defective capacitors.

Pre-bending data was used as a statistical reference for each type of capacitors. Reference response curve with standard deviation intervals was created for each capacitor column by taking the average of the measured acoustic responses. This approach was chosen partly because it provides information on how a certain kind of an intact MLCC typically behaves acoustically, and partly because the measurement setup caused some uncertainties on the measurement data. After the bending, each capacitor on a column was compared to the statistical reference of that capacitor type. One-to-one–comparisons were also made for single capacitors, comparing the acoustic responses of one capacitor before and after bending.
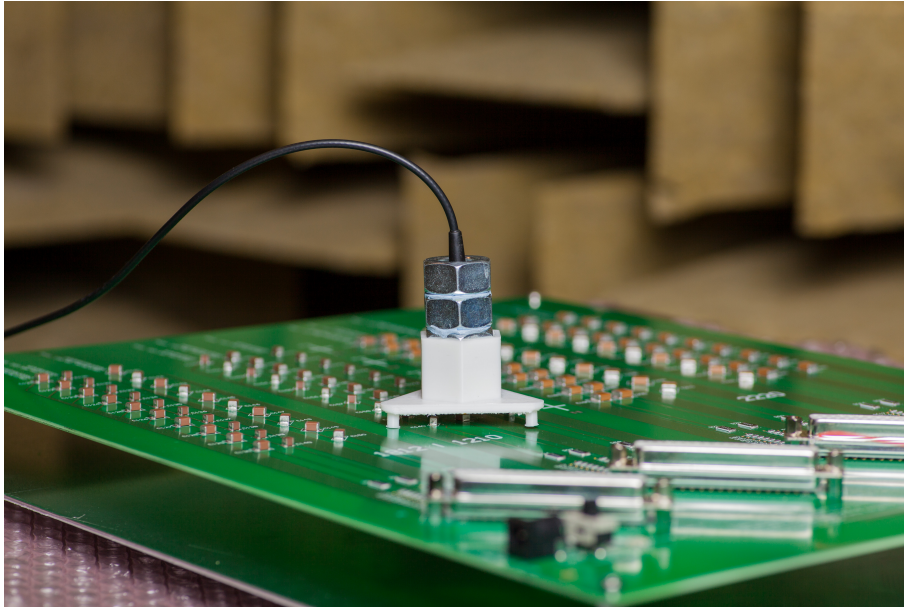
Figure 3.2: KRN point contact sensor with 3D-printed fixture on top of an MLCC

3.4   Test board setup

Several test boards with specifications shown in Table 3.2 were used in the measurements. Labeled as Board 1's and Board 2's, the test boards were structurally identical, with only difference being the capacitor population. The four main variables within the capacitor populations were:

Case size
   1206, 1210, 1812 and 2220 size MLCCs

Orientation
   Angle and location of an MLCC

Termination type
   Standard vs. flex type capacitors

Suppliers
   TDK, AVX and Kemet

An overview of the MLCCs assembled on the test boards is shown in tab 3.3. The MLCCs were assembled on the boards in such way that each column of capacitors has 10 MLCCs of the same case size, type and orientation (figure 3.5). The capacitor populations of the Boards 1 and 2 are shown in Tables 3.4 and 3.5 respectively.
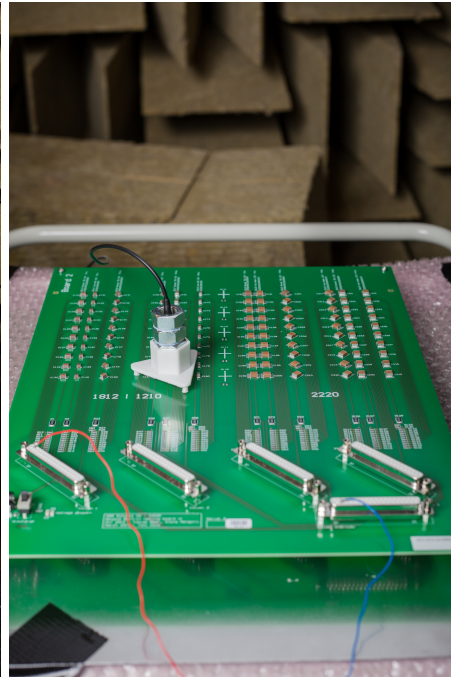
Figure 3.3: Overview of the measurement setup

Figure 3.4: Point contact sensor and PCB

Table 3.2: Test board specifications

Board material	FR-4
Board dimensions	39.0 cm by 30.4 cm
Board thickness	1.55 mm
Number of traces	2
Coatings	none
Type of solder	SAC: 96.5Sn-3.0Ag-0.5Cu

Table 3.3: Overview of the MLCCs assembled on the test boards

| Size	Type	Producer	Code number	Series	V rating	C
1206	Normal	TDK	C2316X7R1E475K160AC	C-series	24 V	4.7 μF
1206	Flex	Kemet	C1206X475K3RACAUTO	FT caps	24 V	4.7 μF
1210	Normal	TDK	C3225X7R1E106M250AC	C-series	24 V	10 μF
1210	Flex	AVX	12103C106M4Z2A	Flexiterm	24 V	10 μF
1210	Flex	Kemet	C1210X106M3RACTU	FT caps	24 V	10 μF
1812	Normal	TDK	C5432X7R1E226M250KC	C-series	24 V	22 μF
2220	Normal	TDK	C5750X7R1E226M250KA	C-series	24 V	22 μF
2220	Flex	Kemet	C2220X226K3RACAUTO	FT caps	24 V	22 μF
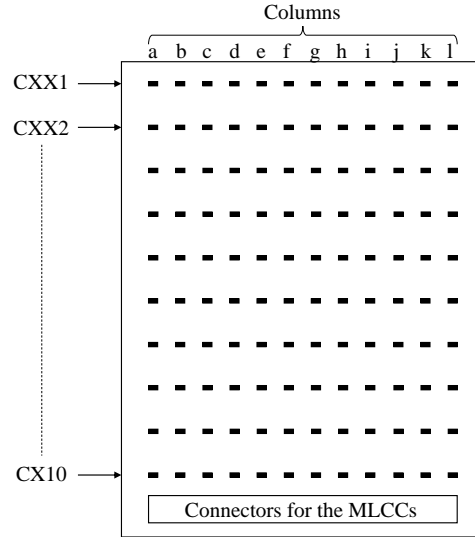
Figure 3.5: Illustration of the placement of the MLCCs on a test board.

Table 3.4: Details about the MLCCs on Board 1

MLCC nr	col	Size	Orientation	Type	Producer	V rating	C
C1-C10	a	1206	0°	Normal	TDK	24 V	4.7 μF
C11-C20	b	1206	0°	Flex	Kemet	24 V	4.7 μF
C21-C30	c	1206	45°	Normal	TDK	24 V	4.7 μF
C31-C40	d	1206	45°	Flex	Kemet	24 V	4.7 μF
C41-C50	e	1206	90°	Normal	TDK	24 V	4.7 μF
C51-C60	f	1206	90°	Flex	Kemet	24 V	4.7 μF
C61-C70	g	1210	0°	Normal	TDK	24 V	10 μF
C71-C80	h	1210	0°	Flex	Kemet	24 V	10 μF
C81-C90	i	1210	45°	Normal	TDK	24 V	10 μF
C91-C100	j	1210	45°	Flex	Kemet	24 V	10 μF
C101-C110	k	1210	90°	Normal	TDK	24 V	10 μF
C111-C120	l	1210	90°	Flex	Kemet	24 V	10 μF

Table 3.5: Details about the MLCCs on Board 2

MLCC nr	col	Size	Orientation	Type	Producer	V rating	C
C121-C130	a	1812	0°	Normal	TDK	24 V	22 μF
C131-C140	b	1210	0°	Flex	AVX	24 V	10 μF
C141-C150	c	1812	45°	Normal	TDK	24 V	22 μF
C151-C160	d	1210	45°	Flex	AVX	24 V	10 μF
C161-C170	e	1812	90°	Normal	TDK	24 V	22 μF
C171-C180	f	1210	90°	Flex	AVX	24 V	10 μF
C181-C190	g	2220	0°	Normal	TDK	24 V	22 μF
C191-C200	h	2220	0°	Flex	Kemet	24 V	22 μF
C201-C210	i	2220	45°	Normal	TDK	24 V	22 μF
C211-C220	j	2220	45°	Flex	Kemet	24 V	22 μF
C221-C230	k	2220	90°	Normal	TDK	24 V	22 μF
C231-C240	l	2220	90°	Flex	Kemet	24 V	22 μF

3.5 Analysis methods for the acoustic data

The number of measured capacitors has to be sufficiently large (dozens or hundreds) to have statistical meaning. The measurement files are also large in size, because the sampling rate of data acquisition must be at least 10 times the highest frequency fed to the capacitor in order to detect these frequencies. Therefore, there is a need for an automatic analysis method which can statistically compare a single measured capacitor to a reference model of this particular type of capacitor.

A method for analyzing MLCC acoustic data was developed. The method is based on obtaining an envelope curve of the measured acoustic response. The use of acoustic envelope provides a smooth curve which neglects phase-differences between measurements whilst maintaining the amplitude information. The envelope curves can be used for one-to-one–comparison and statistical comparison between several envelopes by taking the mean ± standard deviation of multiple envelopes.

A small number of intact and defective capacitors were examined as a preliminary study. By observing the raw measurement data visually, it was noted that a defective MLCC has several characteristic differences compared to an intact MLCC. Such characteristics can be algorithmically detected and include changes in number, location and height of the characteristic peaks of the acoustic response.

The first 1/50th of the measured signal, corresponding to a frequency range of $100\,\mathrm{Hz} - 40\,\mathrm{kHz}$, was cut off from the measurement files because of a high-amplitude burst that occurred in the lower frequencies of the chirp with nearly all of the capacitors. An envelope was then calculated for the signal $u = u(t)$.

Mathematically, the envelope $e(t)$ of a signal $u(t)$ is the modulus of the analytic signal:

$$e(t) = \sqrt{\big(u(t)\big)^2 + Re\left\{\mathcal{H}\big(u(t)\big)\right\}^2}. \tag{3.1}$$

These signals were numerically calculated, and then filtered with 2nd order Butterworth-type lowpass filter with cutoff frequency of 8 kHz. The result was then downsampled with downsampling factor $N_{\mathrm{DS}} = 80$, such that

$$e(t) = \mathrm{Downsample}_{N_{\mathrm{DS}}}\left\{\mathrm{lpf}\left[\sqrt{\big(u(t)\big)^2 + Re\left\{\mathcal{H}\big(u(t)\big)\right\}^2}\right]\right\} \tag{3.2}$$

where $\mathcal{H}(\cdot)$ is the Hilbert transform, and $Re\left\{\mathcal{H}\big(u(t)\big)\right\}^2$ is the so-called analytic signal. The obtained envelope signals $e(t)$ are presented as corresponding frequency domain signals $e(f)$ by scaling the timescale of the measurements with the generator sweep frequency and timespan. It was assumed that the MLCC reacts to changes in the input frequency nearly instantaneously, so the vibration frequency of the MLCC is equal to the signal generator frequency.

Reference envelopes were formed for each capacitor column by calculating the mean

of the acoustic response envelopes of ten intact MLCCs on a column:

$$e_{ref}(f) = \frac{\sum_{n=1}^{10} e_n}{10}.$$ (3.3)

3.5.1 Observation model for the envelope signal

During the experiments, it was observed that the amplitude of the point contact sensor output voltage is slightly dependent on the position, angle and downward force of the point contact sensor. To decrease the effect of these variations, a method of fitting one envelope into another in Least Squares (LS) sense was used. A model where an envelope is fitted into another by multiplying with a scalar is sufficient by following deduction:

Small variations within the mechanical coupling between the sensor and an MLCC are assumed to scale the amplitude of the observed signal by some constant $A > 0$. If $u_1(t)$ and $u_2(t)$ are signals measured from the same MLCC with different levels of mechanical coupling, it holds that

$$u_2(t) = Au_1(t).$$ (3.4)

Envelope curves $e_1(t)$ and $e_2(t)$ are calculated for the signals $u_1(t)$ and $u_2(t)$ as described in Eq. (3.1). Because Hilbert transform is a linear, it holds that for the envelopes

$$e_2(t) = \left|\left|\mathcal{H}\left\{u_2(t)\right\}\right|\right| = \left|\left|\mathcal{H}\left\{Au_1(t)\right\}\right|\right| = \left|\left|A\mathcal{H}\left\{u_1(t)\right\}\right|\right| = Ae_1(t).$$ (3.5)

In addition to the variation of the mechanical contact between the sensor and the MLCC, the electromagnetic interference from the frequency sweep caused distortion in the measurement data. The effect of the EMI is clearly seen in Fig. 4.12 as a somewhat sinusoidal component in the envelopes at frequencies past 1 MHz. This disturbance was observed to be partially caused by the leads that were attached to the connectors of the PCB and the wires on the PCB surface. The noise was also observed to increase in amplitude as the point contact sensor was taken close (~ 1 cm) to the MLCC. An attempt of canceling out the EMI component was made by LS-fitting an envelope of measured EMI into the acoustic response envelopes. This method yielded no successful results, because the EMI component is slightly different at each location and MLCC on a test board. The EMI component is, however, similar with both intact and damaged MLCCs, so it causes no substantial differences between envelopes. Small EMI-related differences between envelopes are partially canceled in calculations by using a method of weighted LS-fitting, shown in (3.6) - (3.13).

3.5.2   Analysis methods

The obtained acoustic response envelopes were inspected both visually and algorithmically for defects:

Visual observations

Visual inspection of the measurement data for changes in the acoustic envelopes between pre- and post-bending measurements. This method was mainly used during the measurements and to verify the calculated values for those capacitors that appeared defective.

GLS-fit and comparison

Perform a generalized least squares fit into the envelope data being examined to compensate for the variation in measurement data amplitude induced by the variations in the measurement setup. Based on eq. (3.5), the fitted model is the reference envelope multiplied with scalar, $e_{\mathrm{ref}} = H\theta + v$, or in matrix form,

$$\begin{pmatrix} e_1 \\ \vdots \\ e_{\mathrm{N}} \end{pmatrix} = \begin{pmatrix} e_{\mathrm{ref},1} \\ \vdots \\ e_{\mathrm{ref},N} \end{pmatrix} (\theta_1) + \begin{pmatrix} v_1 \\ \vdots \\ v_N \end{pmatrix} \tag{3.6}$$

where v is error vector that is assumed to have zero mean (Gaussian distribution), H is the observation matrix and θ is the parameter vector. The fit is calculated with weighting matrix W,

$$W = \mathrm{diag}\left(\frac{1}{\sigma_1^2}, \cdots, \frac{1}{\sigma_N^2} \right) \tag{3.7}$$

where the diagonal elements are the inverse variances of the reference curve. The GLS solution of the parameter vector $\hat{\theta}$ is then obtained by

$$\hat{\theta}_{\mathrm{GLS}} = \left(H^{\mathrm{T}} W H \right)^{-1} H^{\mathrm{T}} W e. \tag{3.8}$$

L_{GLS}-difference value is calculated for an envelope e by calculating squared distances l_i between points e_i and $e_{\mathrm{ref},i}$, scaled with pointwise variances of the reference data:

$$l_i = \frac{1}{\sigma_{\mathrm{ref},i}^2} \left(e_i - \hat{e}_i \right)^2 \tag{3.9}$$

or in matrix form

$$l = W \left(e - \hat{e} \right)^{\mathrm{T}} \left(e - \hat{e} \right) \tag{3.10}$$

The total difference L_{GLS} is obtained by taking the sum of l_i over the mea-

surement sample of N data points and scaling the sum with N

$$\frac{\sum_{i=1}^{N} \frac{1}{\sigma_{\text{ref}}^2} \left(e_i - \hat{e}_i\right)^2}{N}. \tag{3.11}$$

The result is then divided with the mean of fit difference sums $\mu_{L_{GLS},\text{ref}}$ calculated from the individual reference envelopes:

$$L_{GLS} = \frac{\sum_{i=1}^{N} \frac{1}{\sigma_{\text{ref}}^2} \left(e_i - \hat{e}_i\right)^2}{N \mu_{L_{GLS},\text{ref}}}. \tag{3.12}$$

where $\mu_{L_{GLS},\text{ref}}$ is

$$\mu_{L_{GLS},\text{ref}} = \frac{\sum_{k=1}^{n_{\text{ref}}} \left(\frac{\sum_{i=1}^{N} \frac{1}{\sigma_{\text{ref},i} \left(e_{\text{ref}_k,i} - \hat{e}_{\text{ref}_k,i}\right)}}{N} \right)}{n_{\text{ref}}} \tag{3.13}$$

Thus, the value of $L_{GLS} = 1$ corresponds to the reference envelope itself.

Spectrogram analysis

Spectrograms were calculated for certain capacitors to identify the frequency content of observed resonance peaks. Because the input pulse waveform contains a high number of harmonics, the resonance frequencies of an MLCC are excited several times during a frequency sweep. The spectrograms were used to identify the true number of resonant peaks in pre- and post-bending measurements. The spectrograms were calculated using Matlab's `spectrogram()`-function.

4 Results

Comparison of acoustic envelopes before and after bending was made both visually and using the L_{GLS} - algorithm presented in (3.6) - (3.13).

It was observed that nearly all of the MLCCs on bent boards show at least small increase in L_{GLS}-values when compared to those of pre-bending data. Small changes between the pre- and post-bending L_{GLS}-values are likely measurement method-related, whereas significant changes in these values may indicate structural damage in the MLCC.

4.1 Acoustic emission characteristics of damaged MLCCs

A small sample of MLCCs was initially selected for identifying the characteristic changes in the acoustic envelope of a damaged capacitor. The capacitors were selected from two Board 2s, such that one of the boards had been bent, and some MLCCs on it had been identified as defective by electrical analysis. These MLCCs were characterized alongside the corresponding MLCCs on the non-bent board. Figure 4.1 shows an example of typical changes in acoustic envelope of an MLCC that has been structurally damaged. In both pre- and post-bending figures, the obtained data is from the same individual MLCC.

Comparing the measured signal before and after bending in Figs. 4.1a and 4.1b show the typical differences between an intact and a damaged MLCC. With all the MLCCs, regardless the case size and termination type, the most prominent signs of mechanical damage seen in the envelope graphs are

1. Increase in the amplitude of the characteristic peaks

2. Introduction of new peaks, especially at frequencies above 1 MHz

The corresponding numbers 1 and 2 are also marked on figures 4.1a and 4.1b. Additionally, small changes in the resonant frequencies and relative heights of the characteristic peaks were observed in some damaged capacitors. Spectrograms in figures 4.1c and 4.1d show, that the four highest peaks in Fig. 4.1a are actually one resonant frequency at about 0.7 MHz which is also excited by the second, third and fourth harmonic of the pulse wave (see Fig. 3.1 in page 18). In Fig. 4.1b, the peak at 1 MHz is excited by the fundamental frequency of the pulse wave, while the peak at 0.5 MHz appears to consist of both the fundamental frequency and the second harmonic of the pulse wave. The small peak in 4.1b at about 0.65 MHz is excited by the fundamental frequency of the pulse wave.

Based on figures 4.1a - 4.1d, three new resonant frequencies can be detected in the post-bending measurements. This suggests that the MLCC might have suffered multiple different mechanisms of damage. This is also supported by Fig. 4.2. In Fig. 4.2a, a horizontal crack can be seen propagating through the dielectric of the
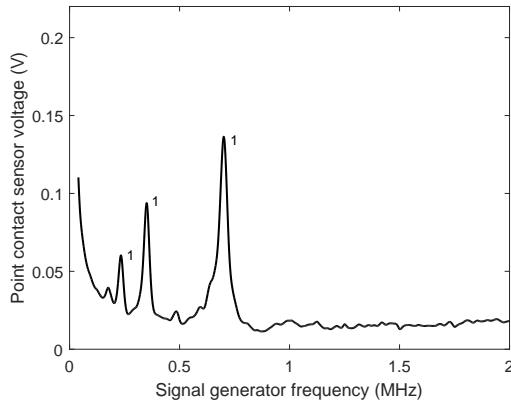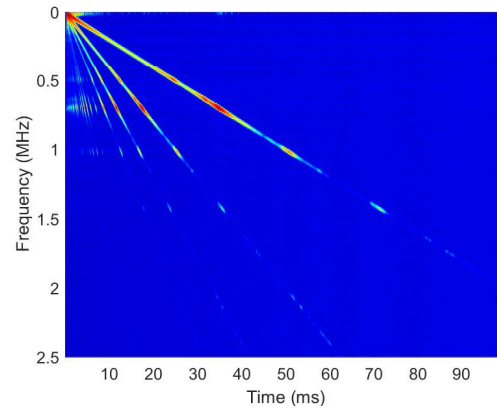
(a) Envelope of acoustic response of an intact capacitor C146
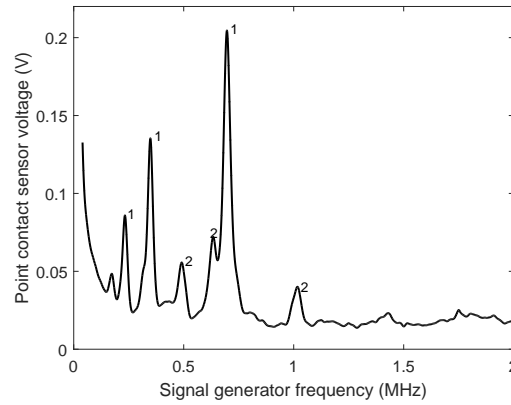
(b) Envelope of acoustic response of the capacitor C146 after bending
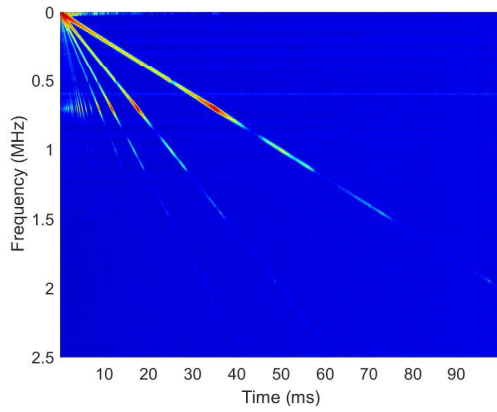
(c) Spectrogram of acoustic response of C146 before bending

(d) Spectrogram of acoustic response of C146 after bending

Figure 4.1: Envelopes and spectrograms of acoustic responses of capacitor C146 (1812 size) before and after bending. The numbers 1 and 2 in (a) and (b) indicate the typical changes in the acoustic response of a damaged capacitor: 1 - amplitude increase in the highest peaks; 2 - emergence of new peaks

MLCC, whereas in both figures 4.2a and 4.2b fractures can be seen in the MLCC close to the end terminations, near the soldering pads. Not all defective MLCCs showed dielectric fractures in X-ray-images, but only near end terminations.

4.2   Statistical analysis of MLCCs before and after bending

Figures 4.3 and 4.4 show the pre- and post-bending histograms of the L_{GLS} values for test boards subjected to 6000 μstr, 5800 μstr and 4300 μstr bending strains. It is clearly seen that the PCB bending procedure affects the obtained acoustic emissions. It is also seen that the range of post-bending L_{GLS} values is significantly
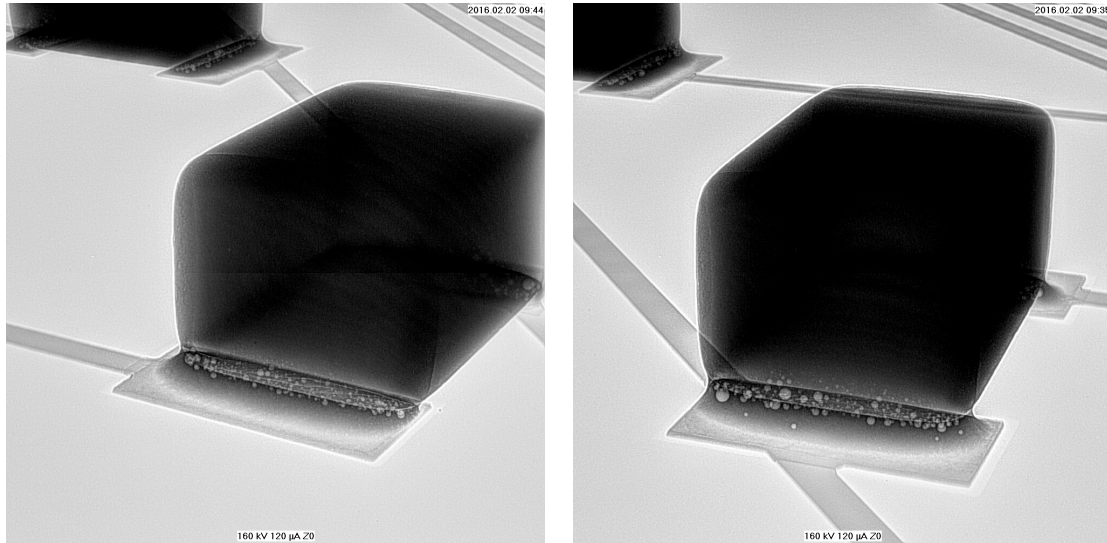
(a) One end termination of C146

(b) Another end termination of C146

Figure 4.2: X-ray images of a damaged MLCC C146 (1812 size). Courtesy of ABB Switzerland Ltd.

different for each case size. Calculated L_{GLS}-values for capacitors on Boards 1 and 2 before and after $4300/5800 \, \mu$str bending are visualized in Figures 4.5a and 4.5b, and Figures 4.6a and 4.6b show the corresponding values for the boards before and after $6000 \, \mu$str bending. Figure 4.7 shows the box plots of the L_{GLS}-values for Boards 1 and 2.

Table 4.1: MLCCs identified as defective by X-ray analysis

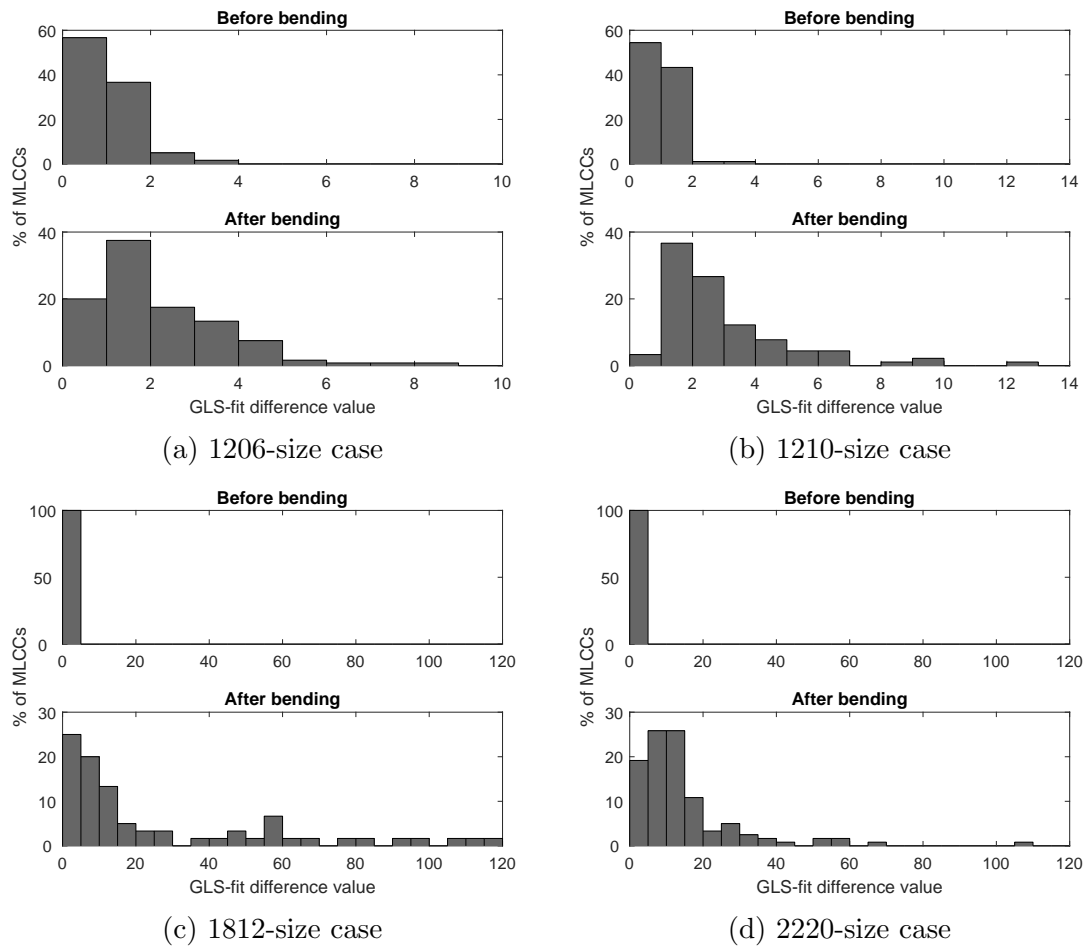| Case size	4300 μstr	5800 μstr	6000 μstr
1206	–	1/60	1/60
1210	0/30	1/60	2/90
1812	15/30	–	20/30
2220	6/60	–	5/60

Figure 4.3: Histograms of L_{GLS}-values for different case size capacitors before and after 6000 μstr bending.
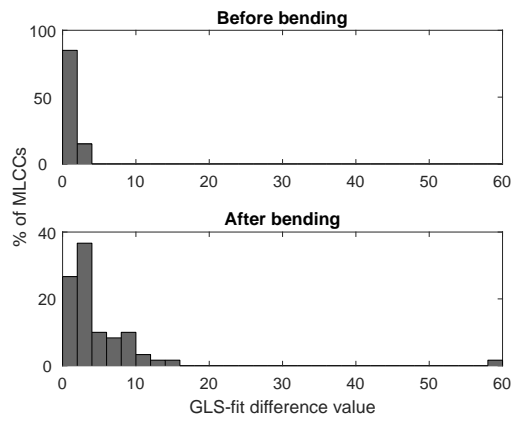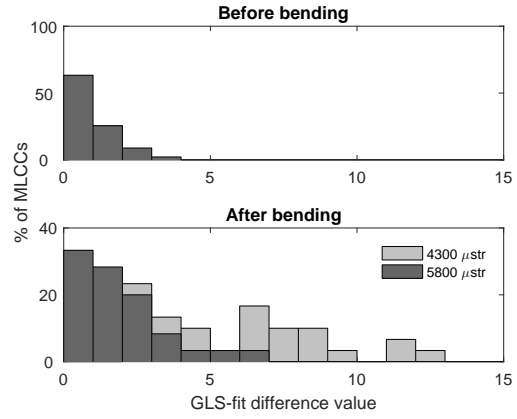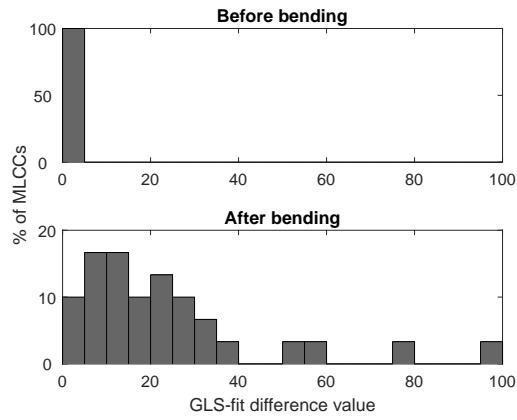
(a) 1206-size case, 5800 μstr bending

(b) 1210-size case, 5800 and 4300 μstr bending

(c) 1812-size case, 4300 μstr bending

(d) 2220-size case, 4300 μstr bending

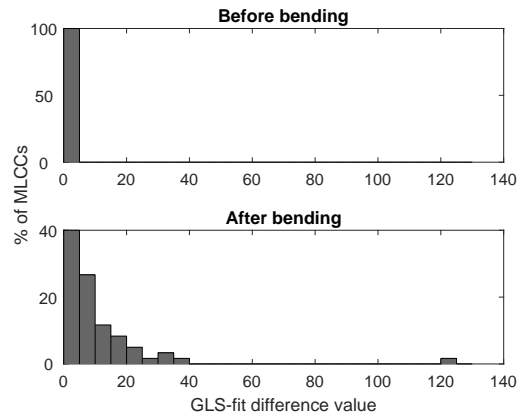Figure 4.4: Histograms of L_{GLS}-values for different case size capacitors before and after 5800/4300 μstr bending.

(a) Board 1   (b) Board 2

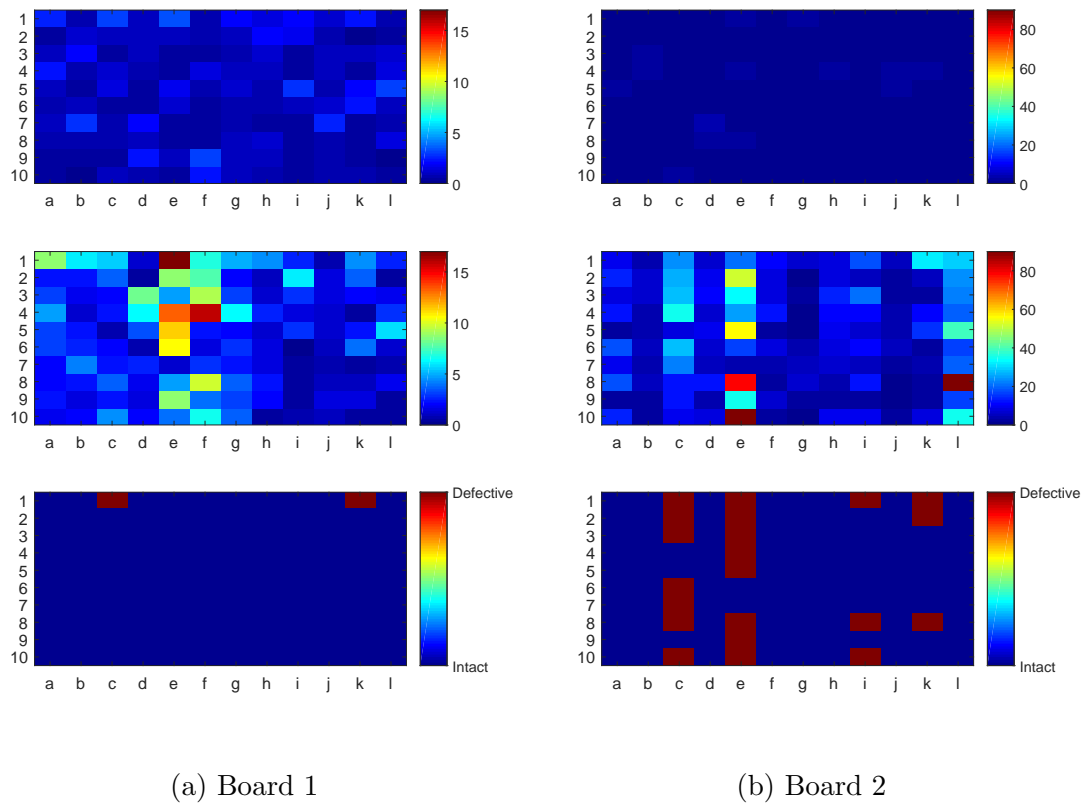Figure 4.5: From top to bottom: Calculated L_{GLS}-values before bending, after 4300/5800 μstr bending, and X-ray analysis results for MLCCs on Boards 1 and 2.

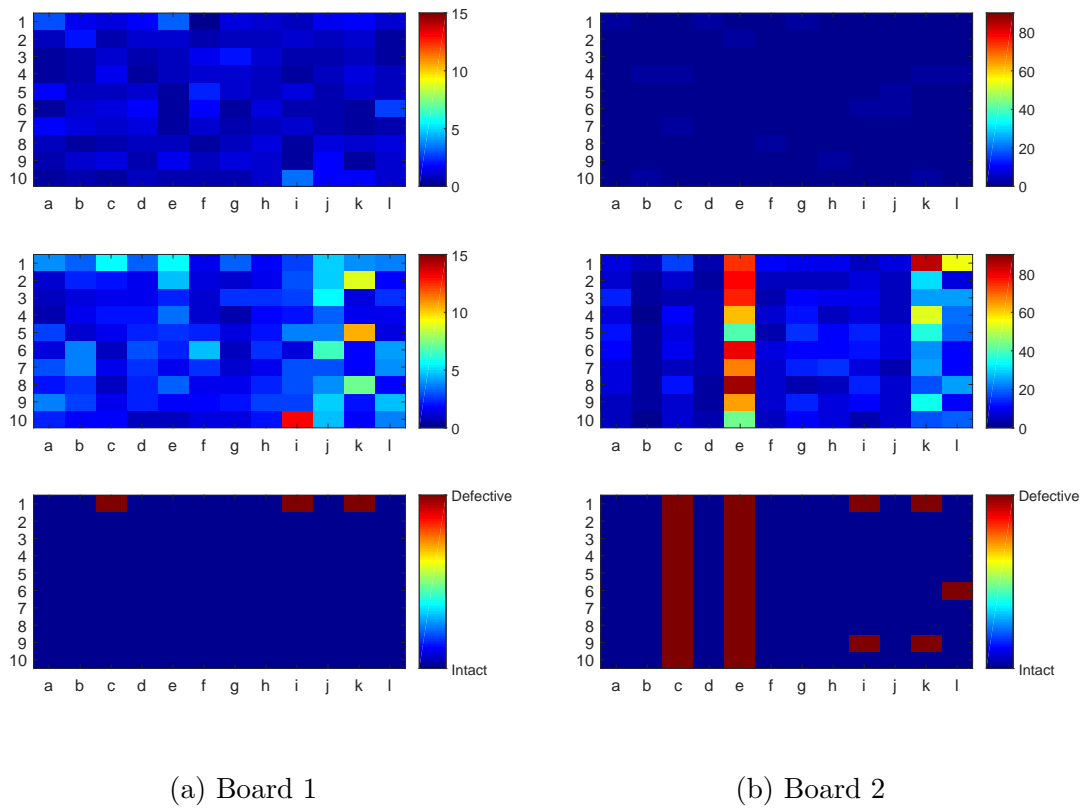(a) Board 1   (b) Board 2

Figure 4.6: From top to bottom: Calculated L_{GLS}-values before bending, after 6000 μstr bending (mean of two measurement runs), and X-ray analysis results for MLCCs on Boards 1 and 2.
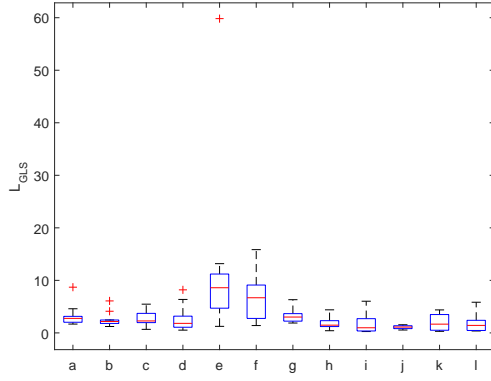
(a) Board 1 after 4300 μstr bending
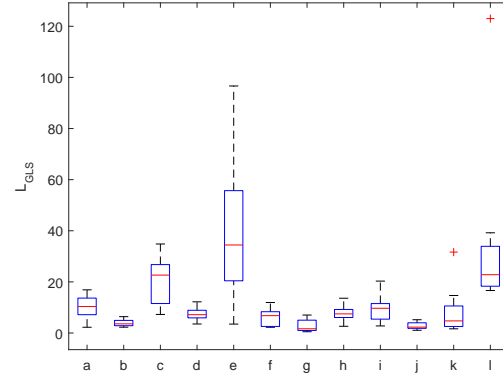
(b) Board 2 after 5800 μstr bending
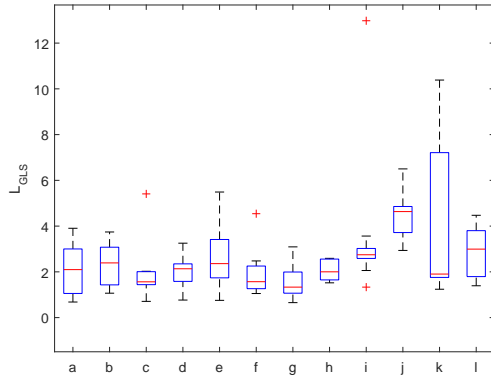
(c) Board 1 after 6000 μstr bending
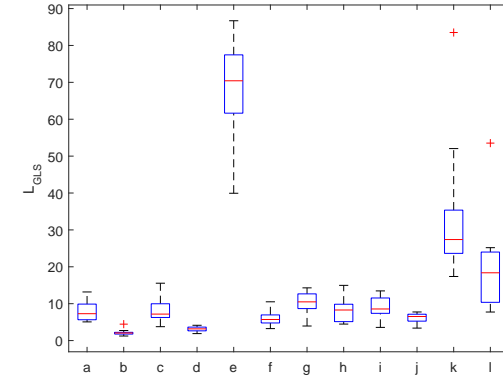
(d) Board 2 after 6000 μstr bending

Figure 4.7: Box plots of L_{GLS}-values per column on Boards 1 and 2. The boxes denote second and third quartile of the data, with red line being the median. The whiskers indicate the range of data. Maximum length of the whiskers is two times the interquartile range. Red "+"–markers outside the whiskers denote outliers.

4.2.1   1206-case MLCCs

Out of the 60 1206-case MLCCs, seen in columns a-f in Fig. 4.6a, only C021 showed signs of damage in the post-bending X-ray analysis. C021 was damaged in both of the boards subjected to 6000 μstr and 5800 μstr bending strain. In Fig. (4.3a), a slight increase in L_{GLS}-values can be seen for 1206-case capacitors, with highest values obtained from C021.

However, the acoustic response of C021 in Fig. 4.8a shows a shift in the resonant frequency of the highest resonance peak from 1.1 MHz to about 1.2 MHz in all pre-and post bending measurements, suggesting that the capacitor might from another manufacturing batch, or already defective during the reference measurements. Spectrogram of C021 in Fig. 4.8b shows that the observed resonance peak is excited by the fundamental frequency of the input signal, not harmonics. Capacitor C001 on another PCB showed similar characteristics to C021 before and after bending.
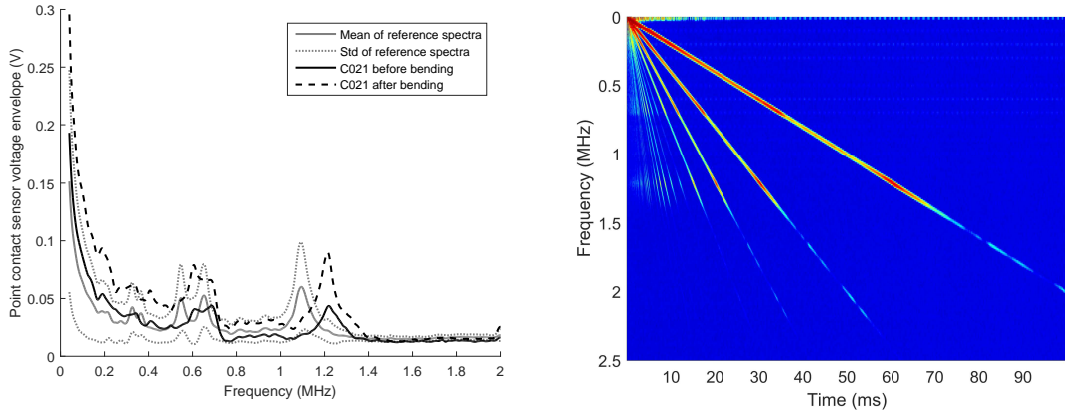
(a) Mean $\pm$ std of acoustic envelopes of capacitors C021-C030 alongside pre- and post-bending acoustic spectrum of C021

(b) Spectrogram of C021 after bending

Figure 4.8: Acoustic response and spectrogram of C021 after 6000 μstr bending

All 1206-case capacitors yielded good acoustic response and signal-to-noise ratio. For flex-termination capacitors, there was a notable differences in resonance peak heights between capacitors both before and after bending. This makes the comparison against averaged envelope more unreliable than with the normal-termination capacitors.

4.2.2   1210-case MLCCs

Table 4.1 shows that no capacitors were damaged on the test board subjected to 4300 μstr bending, and only individual MLCCs were damaged by the higher bending strains, as seen in figures 4.6a (columns g-l) and 4.6b (columns b, d and f).

Damaged capacitor C081 does not show increase in L_{GLS}-values in Fig. 4.6a. Figure 4.9a shows that the envelopes of the MLCC in the pre- and post-bending measurements are almost identical. Similarly, the defective C101 showed very little difference in pre- and post-bending measurements. In Fig. 4.9b, the high standard deviation values in the reference data at 0.65 MHz is caused by acoustic response of C090 which differs from the other reference capacitors on the column.

With all of the 1210-case MLCCs there was variation in the resonant peak heights along a column, both before and after bending. An example of this variation is seen in Fig. 4.10, where all the capacitors on the column could be divided into two sets, one having the highest resonant peak at 0.75 MHz as with C175, and the other at 0.6 MHz as with C175.

(a) C081   (b) C090
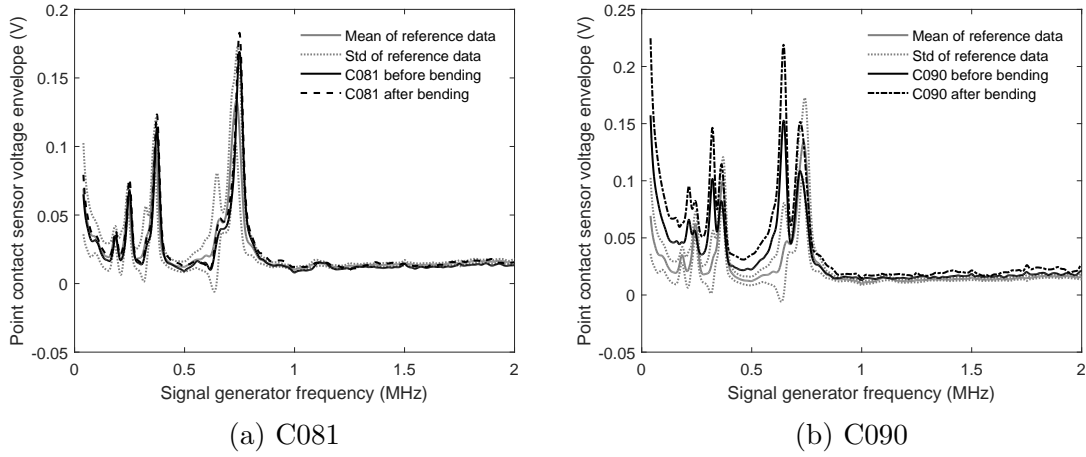
Figure 4.9: Mean ± std of acoustic envelopes of capacitors C081-C090 alongside pre- and post-bending acoustic responses of damaged C081 and non-damaged C90

4.2.3   1812-case capacitors

Majority of the 1812-size MLCCs was damaged by bending, as seen in table 4.1. In the post-6000 μstr-measurements, all the defective MLCCs on col. e are clearly seen in Fig. 4.6b, showing the 1812-case capacitors on columns a, c and e. Col. c yields also distinguishable L_{GLS}-values, although smaller in value than those on col. e. Bending strain of 4300 μstr yielded fewer damaged 1812-case capacitors, with C144, C145 and C149 left intact on column e. These non-damaged MLCCs can be distinguished from the damaged ones in Fig. 4.5b.

The 1812-size capacitors yielded high acoustic response, and the typical changes in the acoustic response can easily be seen in Figs. 4.1a and 4.1b.
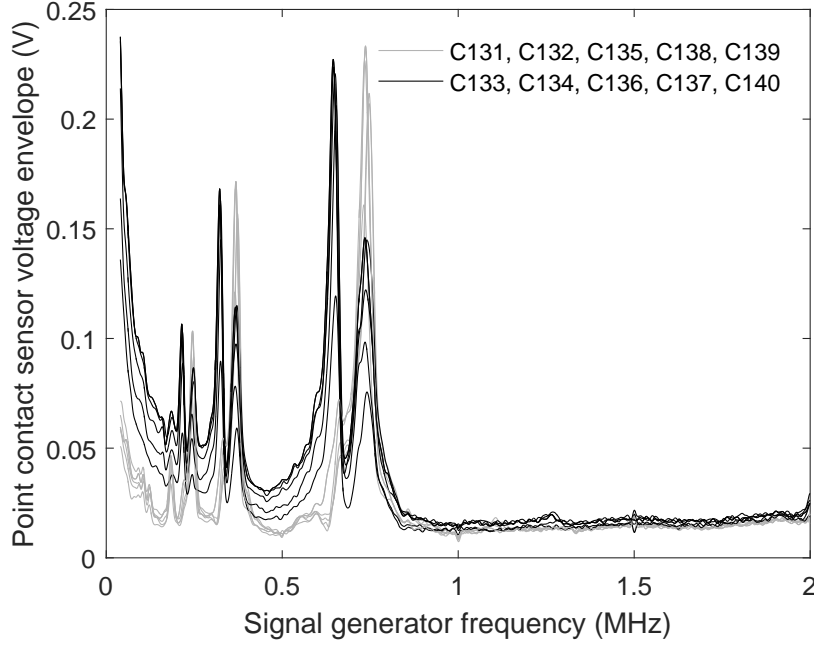
Figure 4.10: Pre-bending acoustic envelopes of all MLCCs on Board 2 column *b*.

4.2.4   2220-case capacitors

Figure 4.11 shows two damaged 2220-size MLCCs. The highest resonance peak of C201 in Fig. 4.11a shows a small frequency shift in post-bending measurements, but the amplitude does not deviate far from the ±Std-limits. The post-bending acoustic envelope of C221 in Fig. 4.11b shows significant increase in both number and height of the resonant peaks.

The 2220-sized MLCCs yielded the lowest acoustic response of the four case sizes, as shown in table 4.2. Figure 4.11a shows that the noise level at the 2 MHz is approximately the same as the reference envelope's resonant peak voltage at 0.5 MHz.

4.3   Comparison of observed acoustic emission amplitudes

The Mean±Std of acoustic emission peak voltages per case size are shown table 4.2. The voltage values are for intact capacitors. Because the amplitude of observed acoustic emission is likely related to the strain (deformation) of the dielectric material in (2.9), the ratios C/A are also provided in the table 4.2.

(a) C201   (b) C221

Figure 4.11: Mean ± std of acoustic responses of C201-210 and C221-C230 alongside damaged MLCCs C201 and C221 before and after bending
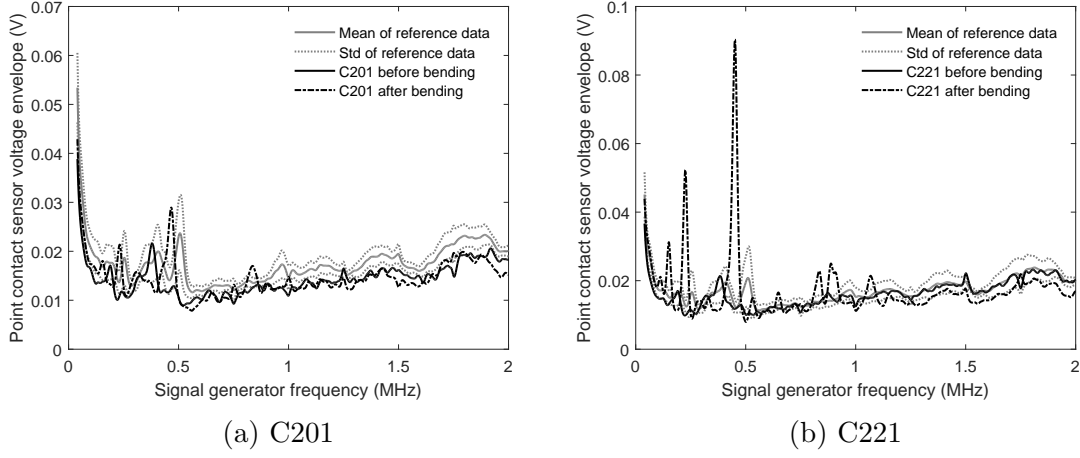
Table 4.2: Capacitances C, surface areas A (Bergenthal, 2016), ratios C/A and Mean±Std for acoustic emission peak voltages for intact MLCCs of different case sizes

Case size	$A\,(\mathrm{mm}^2)$	$C\,(\mu\mathrm{F})$	$\frac{C}{A}\left(\frac{\mu\mathrm{F}}{\mathrm{mm}^2}\right)$	Mean(max$\{e\}$)(V)	Std(max$\{e\}$)(V)
1206	5.12	4.7	0.92	0.0874	0.0247
1210	8.00	10	1.25	0.1588	0.0447
1812	14.40	22	1.52	0.1230	0.0237
2220	28.00	22	0.79	0.0284	0.0052

4.4 Repeatability of the measurements

Repeatability of the measurement method was tested on three columns of intact capacitors and three columns of damaged capacitors. The measured columns were a, b and e on an intact Board 2 and on a Board 2 bent to 4300 μstr. The measured columns were chosen according to results obtained from characterization of the entire Board: column e showed multiple defective MLCCs in the post-bending measurements, whereas capacitors on column b yielded two different types of acoustic response. Column a was chosen as a reference column. Each MLCC was measured five times, detaching the point contact sensor between the measurements.

4.4.1 Error propagation in L_{GLS}-values

The L_{GLS}-values are of the form (3.12), where

$$\hat{e} = H\hat{\theta} = \left(H^{\mathrm{T}}H\right)^{-1} H^{\mathrm{T}}e.$$

If the error of e is at highest δ, then the maximum value of $\hat{\theta}$ including error is

$$\left(H^{\mathrm{T}}H\right)^{-1} H^{\mathrm{T}}(1+\delta)e = (1+\delta)\hat{\theta}.$$

Then the difference $(e - \hat{e})^2$ in (3.12) becomes

$$\begin{aligned}
((1+\delta)e - \hat{e})^2 &= \left((1+\delta)e - (1+\delta)H\hat{\theta}\right)^2 \\
&= (1+\delta)^2 \left(e - H\hat{\theta}\right)^2 \\
&= (1+\delta)^2 \left(e - \hat{e}\right)^2 \\
&= (e - \hat{e}) + \left(\delta^2 + 2\delta\right)(e - \hat{e})
\end{aligned}$$

Thus, the amplitude error δe in e becomes error

$$\left(\delta^2 + 2\delta\right) L_{GLS}$$

in the corresponding L_{GLS}-value.

4.4.2   Errors in measured voltages and L_{GLS}-values

The acoustic response envelope e is assumed to behave as in (3.6), such that the error in measured voltage is of the form δe, $\delta \in \mathbb{R}$. In successive measurements, the δ is assumed to be caused by the inconsistence of the mechanical contact between the sensor and capacitor. Voltage measured at the highest peak of acoustic response was used as a measure of repeatability. Because the acoustic response differs from capacitor to capacitor, Table 4.3 shows the maximum Std:s of mean peak voltages alongside the corresponding relative standard deviations, mean of peak voltages and corresponding δ in L_{GLS} for columns a, b and e on the intact and bent Board 2s. The relative Std:s were used as δ:s when calculating δL_{GLS}:s.

4.5   Effects of PCB vibrations

The possible contribution of the PCB on the capacitor AE measurements was studied by taking reference measurements of the PCB at various distances from the certain MLCC, while driving the capacitor with AC pulse wave sweep (Fig. 4.12). The results show that the PCB vibrates with highest amplitudes in audible frequencies; at a frequency of 50 kHz the measured amplitudes have dropped below the noise floor.

The frequency range of the first resonance modes of the PCB from (2.12), alongside the results in Fig. 4.12, suggest that the board has little to no contribution to the observed acoustic data of the MLCCs near the resonance frequencies of the capacitors.

Table 4.3: Minimum and maximum acoustic response voltages of single MLCCs measured from columns a, b and e on intact and bent Board 2s

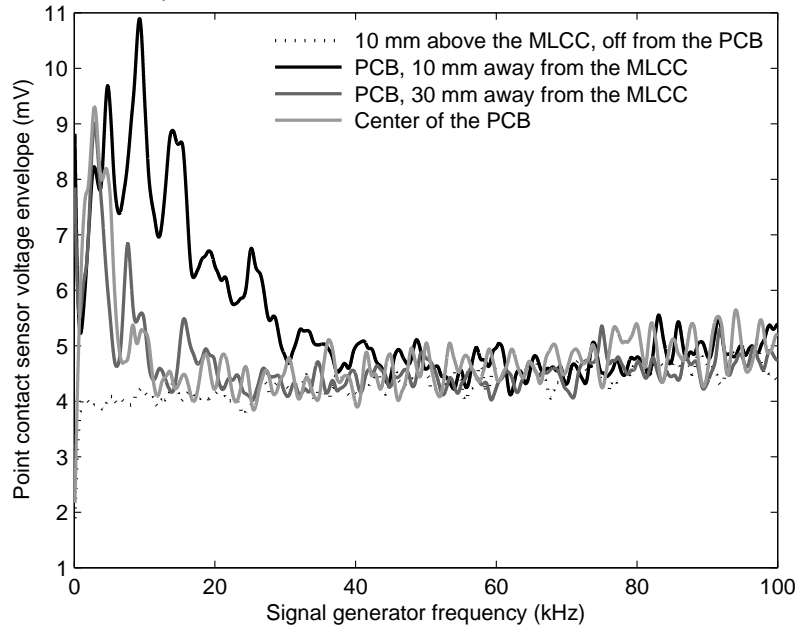| Col	$\max\limits_{i=1,\dots,10}\{\mathrm{Std}\,(e_i)\}$	$\mathrm{Mean}\,(\max\{e_i\})\,(\mathrm{V})$	Relative Std	δL_{GLS}
Intact Board 2				
a	0.0171	0.1683	10.2 %	121.4 %
b	0.0238	0.2221	10.8 %	122.8 %
e	0.0242	0.1560	15.6 %	133.7 %
Bent Board 2				
a	0.0211	0.2089	10.2 %	121.5 %
b	0.0279	0.2798	10.0 %	121.0 %
c	0.0345	0.3072	11.3 %	123.9 %

Figure 4.12: Vibrations measured at various distances away from the MLCC C142 whilst driving the capacitor with AC pulse sweep.

5   Discussion

5.1   Signs of mechanical damage in MLCCs

The results show that subjecting an MLCC to mechanical damage can cause several characteristic changes in its acoustic envelope. Several new resonant peaks in the acoustic response of an MLCC might imply that the capacitor has suffered damage in multiple different locations, and the failure mechanisms may be different. However, it is unclear how the characteristic differences in caused by a termination crack, delamination or crack within the active region of an MLCC differ from one another.

The X-ray images of 1812-sized MLCCs in Figs. 4.2a and 4.2b show cracks both near the end termination and inside the dielectric. It is possible that the solder contacts set conditions for the mechanical vibration amplitude of an MLCC to some degree, and cracks in these locations lead to increased amplitude. Likewise, cracks propagating through the active region of an MLCC might be responsible for new resonant peaks. These are, however, only hypotheses, and would have to be validated by a dedicated study.

5.2 L_{GLS}-values and statistical observations

According to the histograms in Figs. 4.3 and 4.4, most of the MLCCs saw an increase in the calculated L_{GLS}-values. Because the L_{GLS}-calculation compares a single data point to a mean, a small increase in L_{GLS}-values is very likely when the L_{GLS}-values are calculated for data points which are not included in the reference data. The variations within observed acoustic emission amplitudes also cause increase in L_{GLS}-values. Another cause of inaccuracies for L_{GLS}-method is the variation within the reference data, which is mean±std of a set of intact MLCCs. These capacitors should be selected such that all variables, such as manufacturer, batch, capacitance, termination type and case size are the same. However, with some MLCCs, there was two or more different types of acoustic responses found in the reference data. This causes high variation to the reference data, so comparing individual signals with the reference curve becomes more inaccurate.

EMI from the measurement setup causes inaccuracies in the L_{GLS}-values. Typically during a single MLCC column characterization run, the EMI-component in the measured data caused little variance to the acoustic response curves. When the measurement setup is altered, as for example when swapping the test board being inspected, the geometry of the instrument wiring changes, which may cause differences in the observed acoustic response.

5.3   Ability to recognize defects

On Board 1, which housed MLCCs of smaller case sizes, the post-bending L_{GLS}-values were typically between 1 and 4. Columns i and k yielded higher values with higher variance, as seen in Fig. 4.6a. In Fig. 4.6a, the defective 1206-sized C021 is clearly distinguishable from other MLCCs on column c. 1210-sized MLCCs C081 and C101 on columns i and k yield relatively low L_{GLS}-values, and thus cannot be identified as detective by L_{GLS}-values.

On Board 2, defective MLCCs of 1812 size on column e can be clearly seen in Fig. 4.6b. Defective 1812-sized MLCCs on column c yield L_{GLS}-values similar to the 1812-size MLCCs on column a, although no capacitors on column a were identified as defective in the X-ray analysis. Defective 2220-sized capacitors C101 and C109 on column i are not highlighted by the L_{GLS}-values, which likely results from poor acoustic response obtained from the 2220-size capacitors on columns g-j. Columns k and l yielded better acoustic response, which is indicated by higher L_{GLS}-values in Figs. 4.6b and 4.7d. Defective MLCCs C221 and C229 on column k show significantly increased L_{GLS}-values in Fig. 4.6b, whereas C235 on column l yields one of the lowest L_{GLS}-values on the column, and cannot be identified as defective by its L_{GLS}-value.

5.4   Consistence of measurements

The 1812- and 1210-sized MLCCs yielded the strongest acoustic response. The pre- and post-bending response of 1812-sized capacitors was more consistent than 1210-sized capacitors', making the L_{GLS}-comparison more precise for 1812-sized MLCCs. 1210-sized capacitors yielded slightly lower voltages, but the acoustic responses of the 1812-sized capacitors were more consistent, making the algorithmic comparison more accurate. For many of the 1210-sized capacitors, the acoustic envelopes were significantly different from each other, even when comparing capacitors on a single column. Such behavior was observed in both pre- and post-bending measurements, and might be related to capacitors originating from different manufacturing batches.

The 1206-sized MLCCs yielded weaker acoustic response than 1210- and 1812-sized ones, but the obtained acoustic envelopes were more consistent than with the 1210-sized ones. Few 1206-sized MLCCs yielded acoustic envelopes different from others, akin to the 1210-sized ones.

The 2220-case MLCCs proved to be the most difficult case size to measure because of their low acoustic response. In addition, providing sufficient mechanical coupling between sensor and capacitor proved difficult with some of the capacitors, because the top surface of these MLCCs was slightly concave. This case size yielded relatively consistent acoustic envelopes, with no significant difference between capacitors within one column.

The overall acoustic emission amplitudes for different case sizes in table 4.2 appear to somewhat agree with (2.9), which states that the strain in vertical direction in is proportional to capacitance and inversely proportional to capacitor surface area. A high C/A-ratio might explain why the 1210- and 1812-sized MLCCs yield the highest acoustic response. Based solely on (2.9), the 1812-sized capacitors should yield higher acoustic response than 1210-sized MLCCs, but other factors, such as dimensions, mass, material properties and solder joints also contribute to the acoustic response.

6   Conclusions

It was shown that mechanical defects in an MLCC alter the acoustic response of the MLCC, and such defects can be detected using a piezoelectric point contact sensor. The algorithm for defect detection presented in this thesis partially succeeds in recognizing defects in multilayer ceramic capacitors. The biggest challenges of the method are in providing good and repeatable mechanical contact between the point contact sensor and MLCC, and the variation within the reference sample of capacitors.

The mechanical contact issue could be improved by using a point contact sensor with the protective collar removed from surrounding the contact point. The contact point could also be placed on the MLCC more accurately by using a servo-controlled frame for the sensor, for example.

It appears that another kind of data-analysis method would be needed for reliable defect detection method. Although the defect-related changes can often be visually observed from the acoustic response envelope, the L_{GLS}-method often yields "false alarms", because either

(1) The overall amplitudes of the envelopes differ because of variations in the mechanical contact between the sensor and MLCC, or because of the EMI-related component in the measurement data, or

(2) The reference sample contains capacitors with significantly different acoustic responses, resulting in an inaccurate reference envelope with high variance.

Issue (1) could be alleviated by improving the measurement setup as suggested. The contribution of the EMI-component could be reduced by taking a measurement run approximately mm above each MLCC, LS-fitting the observed EMI-component into the acoustic response envelope, and then subtracting the fit. Multiple measurement runs could also be preformed on a single MLCC to obtain an average acoustic response.

Issue (2) would be more difficult to address, because in ideal situation, the reference data would be obtained from the capacitor itself before physical damage occurs. In a production-line application, an acoustic response envelope could be compared with several different reference envelopes, obtained from different batches etc. of a certain type of capacitor.

References

(1949). *IRE Standards on Piezoelectric Crystals.*

(1987). *IEEE Standard on Piezoelectricity.*

(2014). *AMP-1BB-J Broadband Preamplifier Datasheet.* KRN Services.

(2015). *KRNBB-Pc Point Contact Sensor Datasheet.* KRN Services. url: `http://www.krnservices.com/documents/bbpc_flyer_4-13-15.pdf`.

Adams, T. (2014). High Acoustic Frequency Imaging. *Ceramic Industry*, 164(2), pp. 14 – 16. ISSN 00090220, url: `http://search.ebscohost.com/login.aspx?direct=true&db=bth&AN=94147595&site=ehost-live`.

Ahmar, J.A. and Wiese, S. (2015). A Finite Element Modelling and Fracture Mechanical Approach of Multilayer Ceramic Capacitors. In: *16th International Conference on Thermal, Mechanical and Multi-Physics Simulation and Experiments in Microelectronics and Microsystems.*

Bechou, L., Mejdi, S., Ousten, Y., and Danto, Y. (1996). Non-destructive detection and localization of defects in multilayer ceramic chip capacitors using electromechanical resonances. *Quality and reliability engineering international.*

Bergenthal, J. (2016). *Surface Mount - Mounting Pad Dimensions and Considerations.* url: `http://www.kemet.com/Lists/TechnicalArticles/Attachments/29/f2100e.pdf`. KEMET Electronics Corporation.

Chan, Y.C., et al. (1995). Nondestructive detection of defects in miniaturized multilayer ceramic capacitors using digital speckle correlation techniques. *IEEE Transactions on Components, Packaging, and Manufacturing Technology Part A*, 18(3), pp. 677–684. url: `http://search.proquest.com/docview/27455226?accountid=136582`. Last updated - 2011-11-11; SubjectsTermNotLitGenreText - Defects; Correlation methods; Printed circuit boards; Surface mount technology; Nondestructive examination; Cracks; Deformation; Algorithms; Thermal stress; Surface phenomena.

Commare, D.L. (1993). Nondestructive evaluation of MLCCs. *Ceramic Industry*, 140(6), pp. 38–41.

Dahiya, R. (2013). *Robotic Tactile Sensing.* Springer Science+Business Media Dordrecht.

Erdahl, D.S. and Ume, I.C. (2004). Online-Offline Laser Ultrasonic Quality Inspection Tool for Multilayer Ceramic Capacitors-Part I. *IEEE Transactions on Advanced Packaging.*

Furuta, T. and Miura, K. (2010). First-principles study of ferroelectric and piezo-electric properties of tetragonal $SrTiO_3$ and $BaTiO_3$ with in-plane compressive structures. *Solid State Communications*.

Hsueh, C.H. and Ferber, M.K. (2002). Apparent coefficient of thermal expansion and residual stersses in multilayer capacitors. *Composites Part A: applied science and manufacturing*.

Huang, C.W., et al. (2015). Finite Element Analysis and Design of Thermal-Mechanical Stresses in Multilayer Ceramic Capacitors. *International Journal of Applied Ceramic Technology*, 12(2), pp. 451–460. url: `http://search.proquest.com/docview/1660318462?accountid=136582`.

Kahn, S.R. and Checkaneck, R.W. (1983). Acoustic Emission Testing of Multilayer Ceramic Capacitors. *IEEE Transactions on Componenets, Hybrids and Manufacturing Technology*.

Kieran, G.F. (1981). A Comparison of Screening Techniques for Ceramic Capacitors. *Capacitor Technologies, Applications and Reliability; Marshall Space Flight Center*.

Ko, B.H., et al. (2014). Analysis of the correlation between acoustic noise and vibration generated by a multi-layer ceramic capacitor. *Microsyst Technol*.

Krieger, V., et al. (2006). Defect Detection in Multilayer Ceramic Capacitors. *Microelectronics Reliability*.

Lee, T. and Aksay, I.A. (2001). Hierarchial Structure - Ferroelectricity Relationships of Barium Titanate Particles. *Crystal Growth & Design*, 1(5), pp. 401–419. url: `https://www.princeton.edu/~cml/assets/pdf/0105lee_batio3.pdf`.

Levikari, S., et al. (2017). Acoustic detection of cracks and delamination in Multilayer Ceramic Capacitors. In: *2017 IEEE 11th International Symposium on Diagnostics for Electrical Machines, Power Electronics and Drives (SDEMPED)*, pp. 622–627.

Levikari, S., et al. (2018a). Acoustic Phenomena in Damaged Ceramic Capacitors. *IEEE Transactions on Industrial Electronics*, 65(1), pp. 570–577. ISSN 0278-0046, doi:10.1109/TIE.2017.2714123.

Levikari, S., Kärkkäinen, T.J., Andersson, C., and Tamminen, J. (2018b). *MLCC Acoustic Data Set*. url: `http://urn.fi/urn:nbn:fi:csc-kata20180302153714692880`.

Love, A.E.H. (1888). The Small Free Vibrations and Deformation of a Thin Elastic Shell. *Royal Society Publishing*.

Mhamdi, L., Schumacher, T., and Linzer, L. (2015). *Seismology-based acoustic emission techniques for the monitoring of fracture processes in concrete structures.* Woodhead Publishing.

Ousten, Y., et al. (1998). Comparison between piezoelectric method and ultrasonic signal analysis for crack detection in type II multilayer ceramic capacitors. *Quality and reliability engineering international.*

Prymak, J.D. (2006). Piezoelectric Effects Ceramic Chip Capacitors (Singing Capacitors). *Arrow Asian Times.*

Reddy, J.N. (2007). *Theory and analysis of elastic plates and shells.* Boca Raton: CRC Press. ISBN 978-0-8493-8415-8. Previous ed. published: Philadelphia, PA. : Taylor & Francis, c1999, under title: Theory and analysis of elastic plates.

Skelly, A. and Waugh, M.D. (2009). Understanding DC BIAS Characteristics in High-Capacitance MLCCs. *Ceramic Industry*, 159(8), pp. 16 – 18. ISSN 00090220, url: `http://search.ebscohost.com/login.aspx?direct=true&db=bth&AN=45005069&site=ehost-live`.

TDK Corporation (2016). *TDK Techno Magazine - Electronics ABC.* url: `http://www.global.tdk.com/techmag/electronics_primer/vol2.htm`.

Wang, X., Cheng, W., Chan, H., and Choy, C. (2003). H_2O-induced degradation in TiO_2-based ceramic capacitors. *Materials Letters.*

Yang, J. (2005). *An Introduction to the Theory of Piezoelectricity.* Springer.

Zgonik, M., et al. (1994). Dielectric, elastic, piezoelectric, electro-optic, and elasto-optic tensors of $BaTiO_3$ crystals. *Phys. Rev. B*, 50, pp. 5941–5949. doi:10.1103/PhysRevB.50.5941, url: `http://link.aps.org/doi/10.1103/PhysRevB.50.5941`.